Robotica (2017) volume 35, pp. 613–635. © Cambridge University Press 2015
doi:10.1017/S0263574715000739

Unique and accurate soil parameter identification for air-cushioned robotic vehicles

Shuo Xu†,‡,*, Yinan Gu†, Jing Sun† and Dawei Tu†,‡

† *School of Mechatronic Engineering and Automation, Shanghai University, Shanghai 200072, P. R. China*
‡*Shanghai Key Laboratory of Intelligent Manufacturing and Robotics, Shanghai 200072, P. R. China*

(Accepted August 7, 2015. First published online: September 14, 2015)

SUMMARY
On-line identification of soil parameters is a pre-condition of operating performance optimization and control for unmanned ground vehicles (UGV). Inverse calculation from measured vehicular operating parameters is a prevalent methodology. However, it inherently suffers from a multiple-solution problem caused by the coupling of soil parameters in terramechanics equations and an accuracy problem caused by the influences of state noise and measurement noise. These problems in tractive-force-related soil parameters identification were addressed here for air-cushioned vehicles (ACV) by taking advantage of their additional degree of control freedom in vertical force. To be specific, a *g*-function algorithm was proposed to solve the multiple-solution problem from reproductive tractive force equations; de-noising techniques consisting of mean-effect strategies, sampling points selection and sample rearrangement were employed to solve the accuracy problem. A series of experiments were conducted to evaluate these techniques at different noise levels and in different soil conditions. They got satisfactory results in terms of data utilization ratio, identification accuracy and performance stability. The contribution of the paper lies in inventing a novel algorithm for unique and accurate identification of tractive-force-related soil parameters without making any simplification to the original terramechanics equation and with robustness to variations of noise level and soil condition.

KEYWORDS: Soil parameter identification; Terramechanics; Multiple-solution problem; Air-cushioned vehicle (ACV); Unmanned ground vehicle (UGV).

1. Introduction

Environment identification is a pre-condition of operating performance optimization and control for off-road robotic systems. This is specifically necessary for those running on deformable soft terrain where severe sinking of travelling mechanisms (e.g. wheels and tracks) may exist. Accordingly, soil parameters identification for deformable soft terrain constitutes an important branch of the research field of soil/terrain identification. Its theoretical basis is generally built on the terramechanics theory pioneered by Bekker[1,2] and developed by Wong *et al*.[3] In Bekker's terramechanics model, a type of soil is represented by at least eight parameters, which are coupled in, respectively, the equations of tractive force (with three parameters), compaction resistance (with three parameters) and bulldozing resistance (with two parameters) of the travelling mechanism.[4]

Identification methods of soil parameters can be classified into forward calculation and inverse calculation. The procedure of forward calculation is: (1) taking some known soil parameter sets as hypotheses of the current soil; (2) calculating the theoretical values of related vehicular operating parameters from terramechanics equations and vehicular kinematics and dynamics models; (3) measuring the actual values of these vehicular operating parameters and (4) selecting the candidate with the best consistency between the theoretical values and measurements (or a combination of such candidates) as the identification result of the current soil. For example, Ray[5] developed a Bayesian

* Corresponding author. E-mail: sxu@shu.edu.cn

https://doi.org/10.1017/S0263574715000739 Published online by Cambridge University Press

multiple-model estimation method to recursively identify the 8 soil parameters from 21 hypothesized parameter vectors that were published in ref. [3]. Wojciechowski[6] applied an artificial neural network method to solve a simplified 4 parameter identification problem from 36 training sets.

Undoubtedly, the accuracy of forward calculation relies on the quality of the soil hypotheses. A large number of soil hypotheses with a wide parameter distribution must be conductive to compensate for the poor extension capability of forward calculation and improve its robustness in applications. However, such soil conditions are quite limited to be acquired in reality. It is this contradiction that makes Ray[5] attempt to cover the 8-dimensional parameter space via only 21 groups of data. Additionally, due to a loss of consideration of noise, the recursive method in ref. [5] may suffer from a risk of non-convergence when it is used in soil with a large parameter fluctuation.[7–9]

Comparatively, inverse calculation is more popular than forward calculation in soil parameters identification. The philosophy of inverse calculation is calculating the soil parameters from measurements of related vehicular operating parameters by inversely using the terramechanics equations instead of making any hypothesis. However, the number of soil parameters to be identified is larger than that of terramechanics equations (concretely, three parameters are coupled in the tractive force equation, three parameters are coupled in the compaction resistance equation and two parameters are coupled in the bulldozing resistance equation, as referred to above). This will result in a multiple-solution problem[5,10–11] in inverse calculation because different soil parameter combinations can generate the same vehicular operating parameters based on the terramechanics equations. A prevalent methodology to solve the multiple-solution problem is simplifying the terramechanics equations through decoupling the coupled soil parameters.

As tractive force has the greatest impact on vehicular longitudinal motion, the identification of its related three soil parameters (cohesion c, shear deformation modulus K and internal friction angle ϕ) attracts more attention for research. A variety of parameter decoupling methods have been developed correspondingly. For example, Le *et al.*[12] assumed a simplified "force coefficient" model of track-soil interaction. Iagnemma *et al.*[13] only identified cohesion c and internal friction angle ϕ through a linear approximation of the distribution of shear and normal stresses, but set the shear deformation modulus K as a constant. Similarly, c was fixed while only ϕ and K were identified in refs. [11, 14] and a linear stress distribution hypothesis was adopted in refs. [15–17]. It is worth pointing out these simplifications are only reasonable in their given scenarios. For example, the method in ref. [12] is only sound for "rigid-perfectly plastic" soil but not applicable to the targeted deformable soft soil. References [11, 14 and 13] all hypothesized keeping a parameter fixed, but they made a contradictory choice to the fixed parameter; further, these hypotheses all conflict with the measurements published in ref. [3], in which both c and K had a significant change in different types of soil.

Different from above, this work aims to propose a novel methodology of inverse calculation to identify all three tractive force parameters without making any equation simplification, specifically with respect to a novel off-road robotic system – ACV as presented in Fig. 1. As a hybrid vehicle, the weight of the ACV is partly supported by the travelling mechanism (the tracks and guide wheel in Fig. 1) for propulsion and partly supported by the air-cushion (inside the plenum chamber surrounded by the body and flexible skirt) for subsidence prevention. The ratio of the two parts of load is changeable by adjusting rotational speed of the fan. This means, the ACV has an additional degree of control freedom in vertical forces. Various (no less than three) vehicular operating statuses are realizable by taking advantage of this feature, each of which corresponds to a tractive force equation. Then, a numeric algorithm (named "g-function algorithm") is proposed to solve the three soil parameters via the reproductive tractive force equations. Evidently, this inverse calculation method is able to overcome the multiple-solution problem while maintaining the original terramechanics equation without any simplification.

Another innovation of the method lies in solving the identification accuracy problem caused by the influence of noise in the framework of the g-function algorithm. Based on an analysis of noise constitution, a series of de-noising techniques are implemented to reduce noise influence, including: (1) reasonably selecting three (or more) vehicular operating statuses (named "sampling points") according to the established rules; (2) repeatedly sampling around each sampling point to constitute a "sample set" and then conducting mean calculation (in different ways) to counteract the noise within each sample set and (3) rearranging the samples in each sample set and then conducting the subtraction calculations in the g-function algorithm to counteract the noise among the sample sets.

https://doi.org/10.1017/S0263574715000739 Published online by Cambridge University Press

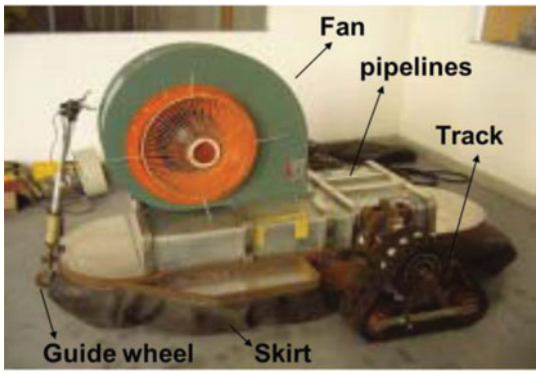


Fig 1. A prototype air-cushioned vehicle.

The remainder of the paper is organized as follows: the *g*-function algorithm and its variants with different mean-effect strategies are proposed in Section 2, selection rules of sampling points are established from a rigorous reasoning in Section 3, sample rearrangement is implemented in Section 4, the complete flowchart for soil parameters identification is then summarized in Section 5, experiments and discussion are conducted in Section 6, and the paper is concluded in Section 7.

2. g-Function Algorithm and Variants in Mean-Effect Strategy

2.1. Problem description

Bekker's tractive force model[2] is given by in Eq. (1). It defines the relationship of tractive force F with soil parameters cohesion c, shear deformation modulus K and internal friction angle ϕ. As referred to above, this paper aims to identify all of the three parameters with neither any equation simplification nor any constant hypothesis to the parameters.

$$F = (Ac + W \cdot \tan\phi)\left[1 - \frac{K}{il}\left(1 - e^{-il/K}\right)\right], \tag{1}$$

where W denotes the weight loaded by a unilateral track, i denotes the slip ratio of the track, l denotes the length of the track and A denotes the track-ground contact area. Vehicular structure parameters l and A are constants. The independent variables in Eq. (1) constitute state set $\boldsymbol{x}$ (using the tangent of ϕ for simplicity) and the measurable signals in Eq. (1) constitute measurement set $\boldsymbol{z}$, i.e.

$$\boldsymbol{x} = [K,\ \tan\phi,\ c,\ W,\ i]^{\mathrm{T}}, \tag{2}$$

$$\boldsymbol{z} = [F,\ W,\ i]^{\mathrm{T}}, \tag{3}$$

where F, W and i are indirectly measured according to the sensory scheme of the prototype ACV. For example, F is transformed from the measurement of the track motor's current, W is transformed from the measurement of the air-cushion pressure or the suspension force and i is derived from the measurements of the driving wheel's rotational speed and the vehicle forward speed. (The readers can refer to ref. [18] for the quasi-static inferring of parameter relationships.) Fluctuations of K, $\tan\phi$ and c and control errors of W and i constitute "state noise" of the state set $\boldsymbol{x}$; as well, sensor errors and transformation errors constitute "measurement noise" of the measurement set $\boldsymbol{z}$. Both categories of noise will bring a negative influence to identification accuracy of the soil parameters, so that de-noising techniques should be introduced to reduce these noise influences.

2.2. g-Function algorithm

In order to realize soil parameters decoupling and identification, no less than three "sampling points" $[F_1, W_1, i_1]$, $[F_2, W_2, i_2]$ and $[F_3, W_3, i_3]$ are selected via the ACV's degrees of control freedom in vertical force and longitudinal motion, where F_p, W_p and i_p denote the soil tractive force, track

https://doi.org/10.1017/S0263574715000739 Published online by Cambridge University Press

load and slip ratio at the p-th sampling point respectively and $p \in \{1, 2, 3\}$. Define $W_1 \geq W_2 \geq W_3$ without a loss of generality. Note that the selection of sampling points should be in accordance with a reasonable manner, see Section 3 for details.

In an idealistic situation with neither state noise nor measurement noise, Eq. (1) is reproduced into Eqs. (4)–(6) with respect to the three sampling points:

$$F_1 = (Ac + W_1 \tan\phi)\left[1 - \frac{K}{i_1 l}\left(1 - e^{-i_1 l/K}\right)\right], \tag{4}$$

$$F_2 = (Ac + W_2 \tan\phi)\left[1 - \frac{K}{i_2 l}\left(1 - e^{-i_2 l/K}\right)\right], \tag{5}$$

$$F_3 = (Ac + W_3 \tan\phi)\left[1 - \frac{K}{i_3 l}\left(1 - e^{-i_3 l/K}\right)\right], . \tag{6}$$

Equations (4)–(6) have no analytical solution for K, $\tan\phi$ and c. Instead, a g-function with respect to the transient variable K (denoted K_t) is constructed for numerical calculation.

$$g(K_t) = \left\{\frac{\frac{F_1}{1-\frac{K_t}{i_1 l}(1-e^{-i_1 l/K_t})} - \frac{F_2}{1-\frac{K_t}{i_2 l}(1-e^{-i_2 l/K_t})}}{W_1 - W_2}\right\} \Bigg/ \left\{\frac{\frac{F_2}{1-\frac{K_t}{i_2 l}(1-e^{-i_2 l/K_t})} - \frac{F_3}{1-\frac{K_t}{i_3 l}(1-e^{-i_3 l/K_t})}}{W_2 - W_3}\right\}. \tag{7}$$

According to ref. [3], the value of K is distributed in the range $[K_{\min}, K_{\max}]$. By assigning values in this range to K_t, the assignment at $g = 1$ is the estimate of K, denoted K_{est}. Substituting K_{est} for K_t in Eqs. (4)–(6) gets the estimates of $\tan\phi$ and c, denoted $\tan\phi_{\text{est}}$ and c_{est}, given by

$$\tan\phi_{\text{est}} = \frac{1}{2}\left(\frac{\frac{F_1}{1-\frac{K_{\text{est}}}{i_1 l}(1-e^{-i_1 l/K_{\text{est}}})} - \frac{F_2}{1-\frac{K_{\text{est}}}{i_2 l}(1-e^{-i_2 l/K_{\text{est}}})}}{W_1 - W_2} + \frac{\frac{F_2}{1-\frac{K_{\text{est}}}{i_2 l}(1-e^{-i_2 l/K_{\text{est}}})} - \frac{F_3}{1-\frac{K_{\text{est}}}{i_3 l}(1-e^{-i_3 l/K_{\text{est}}})}}{W_2 - W_3}\right), \tag{8}$$

$$c_{\text{est}} = \frac{1}{3A}\left(\begin{array}{l}\dfrac{F_1}{1-\frac{K_{\text{est}}}{i_1 l}(1-e^{-i_1 l/K_{\text{est}}})} - W_1\tan\phi_{\text{est}} + \dfrac{F_2}{1-\frac{K_{\text{est}}}{i_2 l}(1-e^{-i_2 l/K_{\text{est}}})} - W_2\tan\phi_{\text{est}} \\ \quad + \dfrac{F_3}{1-\frac{K_{\text{est}}}{i_3 l}(1-e^{-i_3 l/K_{\text{est}}})} - W_3\tan\phi_{\text{est}}\end{array}\right). \tag{9}$$

The above calculation indicates the multiple-solution problem is solved by the g-function algorithm. However, note that the parameter decoupling process relies on a noise-free assumption, which is too idealistic in reality for both state noise and measurement noise. This confliction must damage the identification accuracy of the g-function algorithm and may even result in a fail of identification in extreme cases if K_{est} goes beyond its normal range, or $\tan\phi_{\text{est}}$ or c_{est} gets a negative value.

Although both kinds of noise cannot be eliminated, their impacts on identification accuracy are able to be alleviated by reasonable measures. A commonly-used technique is mean effect by averaging large amounts of measurements to neutralize their random noise. Subsequently, based on different mean-effect strategies, three variants of the g-function algorithm (named $g1$ algorithm, $g2$ algorithm and g-EKF algorithm) are proposed respectively.

2.3. g1 Algorithm

In the $g1$ algorithm, sampling around each sampling point gets the corresponding "sample set" in size s_n. Calculating the mean of the measurements in each sample set gets the input of the g-function algorithm. This mean-effect strategy relies on the hypothesis that the mean of the measurements $\bar{z}$ approximately equals the nominal measurement $\boldsymbol{z}_{\text{nom}}$ with respect to the nominal state $\boldsymbol{x}_{\text{nom}}$, given by

$$\bar{\boldsymbol{z}} = \overline{h(\boldsymbol{x}) + \boldsymbol{e}_z} = \overline{h(\boldsymbol{x})} + \overline{\boldsymbol{e}_z} \approx \overline{h(\boldsymbol{x})} \approx h(\bar{\boldsymbol{x}}) = h(\overline{\boldsymbol{x}_{\text{nom}} + \boldsymbol{e}_x}) \approx h(\boldsymbol{x}_{\text{nom}}) = \boldsymbol{z}_{\text{nom}}, \tag{10}$$

https://doi.org/10.1017/S0263574715000739 Published online by Cambridge University Press

where h denotes the function that maps the state set $\boldsymbol{x}$ to the measurement set $\boldsymbol{z}$, mainly including Eq. (1); $\boldsymbol{e}_x$ and $\boldsymbol{e}_z$ denote state noise and measurement noise respectively.

However, as Eqs. (1) and (4)–(6) are non-linear functions, the measurements of F are non-Gaussian distributed or even asymmetrically distributed even if $\boldsymbol{e}_x$ and $\boldsymbol{e}_z$ are assumed to be Gaussian distributed. This makes the second approximately equal relationship in Eq. (10) not always correct, especially in the case with significant state noise. This is one drawback of $g1$. Another one is the risk of total failure if it gets an ineffective solution ($K_{\text{est}} \notin [K_{\min}, K_{\max}]$ or $\tan\phi_{\text{est}} < 0$ or $c_{\text{est}} < 0$) in the single calling of the g-function algorithm.

2.4. g2 Algorithm

In the $g2$ algorithm, the g-function algorithm is called repeatedly and independently in s_n iterations. Each call employs a sample in each sample set as input and gets an identification result as output. Among the s_n identification results, there exist s_{en} effective results whose mean denotes the final estimate of the soil parameters. This mean-effect strategy relies on the following hypothesis:

$$\begin{aligned}\bar{\boldsymbol{x}} &= \overline{g(\boldsymbol{z}) + \boldsymbol{e}_z} = \overline{g(h(\boldsymbol{x}_{\text{nom}} + \boldsymbol{e}_x) + \boldsymbol{e}_z)} \approx g\left(\overline{h(\boldsymbol{x}_{\text{nom}} + \boldsymbol{e}_x) + \boldsymbol{e}_z}\right) =, g\left(\overline{h(\boldsymbol{x}_{\text{nom}} + \boldsymbol{e}_x)} + \overline{\boldsymbol{e}_z}\right) \\ &= g\left(\overline{h(\boldsymbol{x}_{\text{nom}} + \boldsymbol{e}_x)}\right) \approx g\left(h\left(\overline{\boldsymbol{x}_{\text{nom}} + \boldsymbol{e}_x}\right)\right) = g\left(h(\boldsymbol{x}_{\text{nom}})\right) = \boldsymbol{x}_{\text{nom}}, \end{aligned} \tag{11}$$

where however, owing to the asymmetrical distribution of F_p's measurements, neither of the two approximately equal relationships is correct in situations with either significant state noise or significant measurement noise.

2.5. g-EKF algorithm

In the g-EKF algorithm, an EKF operator is designed to adjust measurements recursively to further neutralize noise on the basis of the $g2$ algorithm. Suppose the current iteration is t, the state transition model and observation model are formulated as below. They are uniform models to all sample sets so that the subscripts 1, 2, 3 are omitted.

$$\boldsymbol{x}(t) = \boldsymbol{x}(t-1) + \boldsymbol{\omega}(t), \tag{12}$$

$$\boldsymbol{z}(t) = h\left(\boldsymbol{x}(t)\right) + \boldsymbol{v}(t), \tag{13}$$

where $\boldsymbol{\omega}(t)$ and $\boldsymbol{v}(t)$ denote the process noise and observation noise in iteration t. They are assumed to be zero mean multivariate Gaussian noise with covariance $\mathbf{Q}$ and $\mathbf{R}$ respectively.

The procedure of the g-EKF algorithm consists of prediction, measurement, measurement correction, g-function calculation and state estimate update. They are introduced step by step.

2.5.1. Prediction. Suppose in the previous iteration, the actual state is $\boldsymbol{x}(t-1)$ with estimate $\hat{\boldsymbol{x}}(t-1)$ and covariance $\mathbf{P}(t-1)$. The predicted state estimate $\hat{\boldsymbol{x}}(t|t-1)$ and predicted state covariance estimate $\mathbf{P}(t|t-1)$ in this iteration are given by

$$\hat{\boldsymbol{x}}(t|t-1) = \hat{\boldsymbol{x}}(t-1), \tag{14}$$

$$\mathbf{P}(t|t-1) = \mathbf{P}(t-1) + \mathbf{Q}. \tag{15}$$

The predicted measurement $\hat{\boldsymbol{z}}(t|t-1)$ and its covariance $\mathbf{P}_z(t|t-1)$ can be derived from $\hat{\boldsymbol{x}}(t|t-1)$ by Eqs. (16)–(18), in which $\mathbf{H}(t)$ is a Jacobian matrix to linearize the relationship of $\boldsymbol{z}$ and $\boldsymbol{x}$.

$$\hat{\boldsymbol{z}}(t|t-1) = h\left(\hat{\boldsymbol{x}}(t|t-1)\right), \tag{16}$$

$$\mathbf{H}(t) = \left.\frac{\partial \boldsymbol{z}}{\partial \boldsymbol{x}}\right|_{\hat{x}(t|t-1)}, \tag{17}$$

$$\mathbf{P}_z(t|t-1) = \mathbf{H}(t)\mathbf{P}(t|t-1)\mathbf{H}(t)^T. \tag{18}$$

https://doi.org/10.1017/S0263574715000739 Published online by Cambridge University Press

2.5.2. Measurement. The actual measurement is denoted $z(t)$. Its residual with the predicted measurement $\hat{z}(t|t-1)$ is denoted $\hat{\boldsymbol{y}}(t)$ with covariance $\mathbf{S}(t)$. $\hat{\boldsymbol{y}}(t)$ and $\mathbf{S}(t)$ are given by

$$\hat{\boldsymbol{y}}(t) = z(t) - \hat{z}(t|t-1), \tag{19}$$

$$\mathbf{S}(t) = \mathbf{P}_z(t|t-1) + \mathbf{R} = \mathbf{H}(t)\mathbf{P}(t|t-1)\mathbf{H}(t)^T + \mathbf{R}. \tag{20}$$

2.5.3. Measurement correction. Different from standard EKF, the measurement rather than the state estimate is corrected here. To be specific, $z(t)$ is adjusted by $\hat{z}(t|t-1)$ to obtain a more precise measurement estimate $\hat{z}(t)$ with smaller covariance $\mathbf{P}_z(t)$, given by

$$\mathbf{K}(t) = \mathbf{P}_z(t|t-1)\mathbf{S}(t)^{-1}, \tag{21}$$

$$\hat{z}(t) = \hat{z}(t|t-1) + \mathbf{K}(t)\hat{\boldsymbol{y}}(t), \tag{22}$$

$$\mathbf{P}_z(t) = (\mathbf{I} - \mathbf{K}(t))\mathbf{P}_z(t|t-1), \tag{23}$$

where $\mathbf{K}(t)$ denotes the Kalman gain, which represents the extent of the belief in measurement relative to prediction; $\hat{z}(t)$ denotes the corrected measurement, which acts as the estimate of actual vehicular signals and $\mathbf{P}_z(t)$ denotes the corrected measurement covariance.

2.5.4. g-function calculation. $\hat{z}_1(t)$, $\hat{z}_2(t)$ and $\hat{z}_3(t)$ are input into Eqs. (7)–(9) to identify the soil parameters $K_{\text{est}}(t)$, $\tan\phi_{\text{est}}(t)$ and $c_{\text{est}}(t)$. As noted before, if $K_{\text{est}}(t)$ is outside its normal range, or $\tan\phi_{\text{est}}(t)$ or $c_{\text{est}}(t)$ is negative, the identification result is deemed invalid. In this case, the subsequent step "state estimate update" is skipped and the estimates of state and state covariance are set to the values in the previous iteration (i.e. $\hat{\boldsymbol{x}}(t) = \hat{\boldsymbol{x}}(t-1)$, $\mathbf{P}(t) = \mathbf{P}(t-1)$). Otherwise, state estimate update is carried out as follows.

2.5.5. State estimate update. After measurement correction and g-function calculation, the state estimate $\hat{\boldsymbol{x}}(t)$ is given by

$$\hat{\boldsymbol{x}}(t) = [K_{\text{est}}(t),\ \tan\phi_{\text{est}}(t),\ c_{\text{est}}(t),\ \hat{W}(t), \hat{i}(t)]^T. \tag{24}$$

Note that the steps of prediction, measurement and measurement correction (i.e. Eqs. (10)–(22)) are implemented separately for different sample sets on purpose of reducing matrix size and computational burden. Instead, the update of state covariance estimate $\mathbf{P}(t)$ should be processed in an integrative manner because a part of its uncertainty is transferred from $\mathbf{P}_z(t)$ through the g-function, which merges measurements of all sample sets. An extended measurement set is denoted $z_{\text{e}} = [{z_1}^T, {z_2}^T, {z_3}^T] = [F_1, W_1, i_1, F_2, W_2, i_2, F_3, W_3, i_3]^T$ with estimate $\hat{z}_{\text{e}}$ and covariance $\mathbf{P}_{z\text{e}}(t)$. $\mathbf{P}_{z\text{e}}(t)$ is a 9*9-ordered block triangular matrix that integrates $\mathbf{P}_{z1}(t)$, $\mathbf{P}_{z2}(t)$ and $\mathbf{P}_{z3}(t)$. z_{e} is further extended to z_{e1} by merging K. z_{e1} and its estimate $\hat{z}_{\text{e1}}$ are given by

$$z_{\text{e1}} = [z_{\text{e}}^{\text{T}}, K]^{\text{T}} = [F_1, W_1, i_1, F_2, W_2, i_2, F_3, W_3, i_3, K]^{\text{T}}, \tag{25}$$

$$\hat{z}_{\text{e1}}(t) = [\hat{z}_{\text{e}}(t)^{\text{T}}, K_{\text{est}}(t)]^{\text{T}}. \tag{26}$$

The corresponding extended covariance (denoted $\mathbf{P}_{z\text{e1}}(t)$) is a block matrix, given by

$$\mathbf{P}_{z\text{e1}}(t) = \begin{bmatrix} \mathbf{P}_{z\text{e}}(t) & \vdots & \left(\left.\frac{dK_{\text{est}}}{dz_{\text{e}}}\right|_{\hat{z}_{\text{e}}(t)} \cdot \text{diag}\,(\mathbf{P}_{z\text{e}}(t))\right)^{\text{T}} \\ \cdots & \vdots & \cdots \\ \left.\frac{dK_{\text{est}}}{dz_{\text{e}}}\right|_{\hat{z}_{\text{e}}(t)} \cdot \text{diag}\,(\mathbf{P}_{z\text{e}}(t)) & \vdots & \text{var}\,(K_{\text{est}}(t)) \end{bmatrix}_{10\times 10}, \tag{27}$$

https://doi.org/10.1017/S0263574715000739 Published online by Cambridge University Press

where the custom function diag(*) is used to pick the diagonal elements of a matrix; var($K_{\text{est}}(t)$) denotes the variance of $K_{\text{est}}(t)$, given by

$$\text{var}\left(K_{\text{est}}(t)\right) = \left.\frac{dK_{\text{est}}}{dz_{\text{e}}}\right|_{\hat{z}_{\text{e1}}(t)} \cdot \mathbf{P}_{z\text{e}}(t) \cdot \left(\left.\frac{dK_{\text{est}}}{dz_{\text{e}}}\right|_{\hat{z}_{\text{e1}}(t)}\right)^{\text{T}}, \tag{28}$$

where owing to a lack of an explicit relationship between K_{est} and z_{e}, the derivative $dK_{\text{est}}/dz_{\text{e}}$ is calculated via the implicit function theorem, *viz.*

$$\left.\frac{dK_{\text{est}}}{dz_{\text{e}}}\right|_{\hat{z}_{\text{e1}}(t)} = -\left.\frac{\partial(g-1)/\partial z_{\text{e}}}{\partial(g-1)/\partial K_t}\right|_{\hat{z}_{\text{e1}}(t)}, \tag{29}$$

where the numerator and denominator of the expression on the right side of the equal sign are computable from Eq. (7) because g (and also g –1) is a function with respect to both K_t and z_{e}, and $g - 1 = 0$ at $K_t = K_{\text{est}}(t)$ and $z_{\text{e}} = \hat{z}_{\text{e}}(t)$.

Similarly, the variance of tan$\phi_{\text{est}}(t)$ is derived in Eq. (30), where the derivative $d(\tan\phi_{\text{est}})/dz_{\text{e1}}$ is computable from Eq. (8).

$$\text{var}\left(\tan\phi_{\text{est}}(t)\right) = \left.\frac{d(\tan\phi_{\text{est}})}{dz_{\text{e1}}}\right|_{\hat{z}_{\text{e1}}(t)} \cdot \mathbf{P}_{z\text{e1}}(t) \cdot \left(\left.\frac{d(\tan\phi_{\text{est}})}{dz_{\text{e1}}}\right|_{\hat{z}_{\text{e1}}(t)}\right)^{\text{T}}. \tag{30}$$

Next, $\mathbf{P}_{z\text{e2}}(t)$, var($c_{\text{est}}(t)$) and $\mathbf{P}_{z\text{e3}}(t)$ are calculated successively by taking reference the method of Eqs. (27) and (30). The acquired 12*12-ordered extended covariance $\mathbf{P}_{z\text{e3}}(t)$ is partitioned to a block matrix:

$$\mathbf{P}_{z\text{e3}}(t) = \begin{bmatrix} \mathbf{P}_{z\text{e}}(t) & \vdots & \mathbf{B}_{9\times3} \\ \cdots & \vdots & \cdots \\ \mathbf{C}_{3\times9} & \vdots & \mathbf{D}_{3\times3} \end{bmatrix}_{12\times12}, \tag{31}$$

where $\mathbf{D}$ denotes the covariance of soil parameter estimates; $\mathbf{B}$ denotes the covariance between measurements and soil parameter estimates; and $\mathbf{C} = \mathbf{B}^T$.

Finally, the updated state covariance estimate $\mathbf{P}(t)$ is extracted from $\mathbf{P}_{z\text{e3}}(t)$ with respect to each sample set.

$$\mathbf{P}(t) = \begin{bmatrix} \mathbf{D}_{3\times3} & \vdots & \mathbf{E}_{3\times2} \\ \cdots & \vdots & \cdots \\ \mathbf{F}_{2\times3} & \vdots & \mathbf{G}_{2\times2} \end{bmatrix}, \tag{32}$$

where $\mathbf{G}$ is the sub-matrix of $\mathbf{P}_{z\text{e}}(t)$ with respect to W_p and i_p, $p \in \{1, 2, 3\}$; $\mathbf{E}$ and $\mathbf{F}$ are composed of the corresponding elements of $\mathbf{C}$ and $\mathbf{B}$.

This iteration is completed so far. Then, the next iteration starts to run until all of the s_n groups of samples are processed. Suppose s_{en} effective identification results are preserved from the s_n identification results, their mean denotes the final estimate of the soil parameters.

3. Sampling Points Selection

3.1. Intention and strategies of sampling points selection

In addition to the mean-effect strategies, reasonably selecting sampling points is a second technique to reduce the influence of noise on accuracy for the g-function algorithm. It is applicable to $g1$, $g2$ and g-EKF.

https://doi.org/10.1017/S0263574715000739 Published online by Cambridge University Press

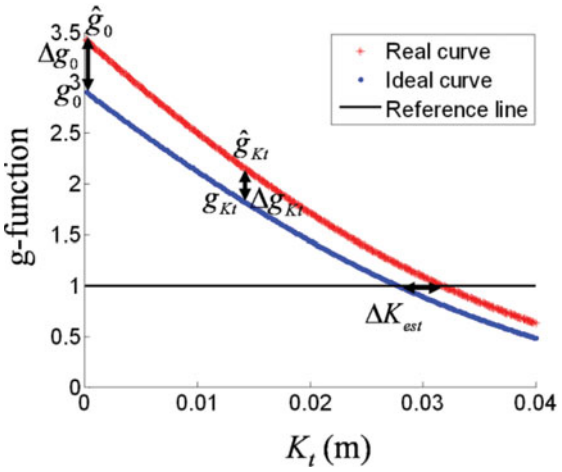


Fig 2. Illustration of K's estimation error.

According to Eq. (3), a combination of soil tractive force F, track load W and slip ratio i in a vehicular operating status constitutes a sampling point. Further, according to Eq. (1), F is the function of W and i (as well as the soil parameters). Therefore, selecting three sampling points (as required by the g-function algorithm, see Section 2.2) is actually selecting three combinations of W and i.

A straightforward idea is enlarging the distances between the sampling points because this can make noise-caused data fluctuation within each sample set relatively less evident than the differences between the sample sets and thus weaken the impact of noise on identification accuracy. As W_p is positively correlated with F_p where $p \in \{1, 2, 3\}$, it gives $W_1 \gg W_2 \gg W_3$ in order to make $F_1 \gg F_2 \gg F_3$, namely, $W_1 > W_2 > W_3$ with a clear gap. (Similarly, the sign $\ll$ denotes "smaller with a clear gap".) Further, without a loss of generality, let $(W_2 - W_3)/(W_1 - W_2) = 1$ for simplification. Note that this assignment of value is not an essential condition, see Section 3.4. The resultant selection rule of sampling points is given by

$$Rule1 : (W_2 - W_3)/(W_1 - W_2) = 1, \quad \text{and } W_1 \gg W_2 \gg W_3.$$

The relationships of i_1, i_2 and i_3 will be reasoned next. Since identifying K is a basis of identifying $\tan\phi$ and c in the g-function algorithm (see Eqs. (8) and (9)), the subsequent discussion concentrates on K on purpose of reducing its estimation error ΔK_{est}. An example is shown in Fig. 2, in which the horizontal axis denotes K_t (i.e. the transient K value) and the vertical axis denotes the g-function values (i.e. g_{Kt} for the ideal curve without noise and $\hat{g}_{Kt}$ for the actual curve with noise). Their difference Δg_{Kt} ($\Delta g_{Kt} = \hat{g}_{Kt} - g_{Kt}$) represents the influence of noise. Intersections of the curves with the reference line ($g = 1$) denote K's nominal value K_{nom} and estimate K_{est} respectively. At the left end where $K_t = 0$, the initial g-function values are denoted g_0 and $\hat{g}_0$ and the corresponding initial error is given by $\Delta g_0 = \hat{g}_0 - g_0$. Note that the ideal curve may also be on top of the actual curve, but their relative position does not affect the subsequent reasoning.

Intuitively, the following three strategies are expected to be conductive to reduce ΔK_{est} in determining the sampling points:

(1) Enlarging $(g_0 - 1)$ on purpose of enlarging the "safety margin" against noise;
(2) Diminishing the ratio $|\Delta g_0|/(g_0 - 1)$ (denoted $|\Delta g_0\%|$) on purpose of diminishing the magnitude of the initial error relative to the safety margin; and
(3) Ensuring $|\Delta g_{Kt}| < |\Delta g_0|$ on purpose of narrowing the gap between the actual curve and the ideal curve as K_t increases.

The relationships of i_1, i_2 and i_3 will be reasoned in these three perspectives subsequently.

https://doi.org/10.1017/S0263574715000739 Published online by Cambridge University Press

3.2. Selecting sampling points to increase g_0

Referring to Eq. (7), the equivalent soil tractive force F_t with respect to K_t is defined as

$$F_t(K_t) = \frac{F}{1 - \frac{K_t}{il}(1 - \mathrm{e}^{-il/K_t})}. \tag{33}$$

It gives $F_t(K_t) = F$ iff $K_t = 0$. We define a simplified expression of $F_t(0)$ as F_0; evidently, $F_0 \propto W$ and $F_0 \propto i$. Based on Eq. (7), the initial ideal g-function value g_0 is given by

$$g_0 = \frac{(F_{01} - F_{02})/(W_1 - W_2)}{(F_{02} - F_{03})/(W_2 - W_3)} = \frac{F_{01} - F_{02}}{F_{02} - F_{03}}, \tag{34}$$

where F_{0p} ($p \in \{1, 2, 3\}$) denotes the corresponding F_0 to the three sampling points.

Equation (34) indicates g_0 is positively correlated with F_{01} and F_{03} but negatively correlated with F_{02}. As F_{0p} is positively correlated with i_p (derived from Eqs. (4)–(6)), g_0 is thus positively correlated with i_1 and i_3 but negatively correlated with i_2. Accordingly, the relationships $i_1 \gg i_2$ and $i_3 \gg i_2$ should be beneficial to increasing g_0 in a straightforward perspective. Concretely, their effects on increasing g_0's numerator (denoted $g_{0,n}$) and decreasing its denominator (denoted $g_{0,d}$) are explored as follows.

Based on Eqs. (34) and (4)–(6), $g_{0,n}$ is given by

$$\begin{aligned} g_{0,n} = F_{01} - F_{02} = \tan\phi(W_1 - W_2) + \frac{KAc}{l}\left[\frac{1}{i_2}(1 - \mathrm{e}^{-i_2 l/K}) - \frac{1}{i_1}(1 - \mathrm{e}^{-i_1 l/K})\right] \\ + \frac{K\tan\phi}{l}\left[\frac{W_2}{i_2}(1 - \mathrm{e}^{-i_2 l/K}) - \frac{W_1}{i_1}(1 - \mathrm{e}^{-i_1 l/K})\right], \end{aligned} \tag{35}$$

where the first item of the expression on the right side of the equal sign is a positive constant that acts as a bias to ensure $g_{0,n}$ is positive. In the second item, we define $f(i) \triangleq (1 - \mathrm{e}^{-il/K})/i$. As $f(i)$ is negatively correlated with i, the second item is positive iff $i_1 > i_2$ and a large gap between i_1 and i_2 is preferred. In the third item, we define $f(i_1, i_2) \triangleq W_2(1 - \mathrm{e}^{-i_2 l/K})/i_2 - W_1(1 - \mathrm{e}^{-i_1 l/K})/i_1$. Its partial derivatives with respect to i_1 and i_2 are given by

$$\frac{\partial f(i_1, i_2)}{\partial i_1} = \frac{W_1}{i_1^2}\left(1 - \mathrm{e}^{-i_1 l/K} - \frac{i_1 l}{K}\mathrm{e}^{-i_1 l/K}\right) > 0, \tag{36}$$

$$\frac{\partial f(i_1, i_2)}{\partial i_2} = -\frac{W_2}{i_2^2}\left(1 - \mathrm{e}^{-i_2 l/K} - \frac{i_2 l}{K}\mathrm{e}^{-i_2 l/K}\right) < 0. \tag{37}$$

They mean the third item is positively correlated with i_1 but negatively correlated with i_2, so that a large value of i_1/i_2 is preferred. As the third item is negative at the specific assignments, $i_1/i_2 = 1$ and $i_1/i_2 = W_1/W_2$, the bigger value is set as the lower limit of the ratio of i_1 to i_2.

To sum up, in the perspective of increasing $g_{0,n}$, the preferred relationship between i_1 and i_2 is given by

$$Rule2 : i_1 \gg i_2, \text{ at least } i_1 \geq i_2 \cdot W_1/W_2.$$

Similarly, the following rule is established for i_2 and i_3 in the perspective of reducing $g_{0,d}$

$$Rule3 : i_2 \ll i_3, \text{ at least } i_2 < i_3.$$

3.3. Selecting sampling points to reduce $|\Delta g_0\%|$

Taking noise into consideration, $\hat{g}_0$ (the actual g-function value at $K_t = 0$) is given by

$$\hat{g}_0 = \frac{(\hat{F}_{01} - \hat{F}_{02})/(W_1 - W_2)}{(\hat{F}_{02} - \hat{F}_{03})/(W_2 - W_3)} = \frac{F_{01}(1 + e_1) - F_{02}(1 + e_2)}{F_{02}(1 + e_2) - F_{03}(1 + e_3)}, \tag{38}$$

https://doi.org/10.1017/S0263574715000739 Published online by Cambridge University Press

where e_1, e_2 and e_3 denote the percentage errors in F_1, F_2 and F_3 respectively under a synthesized effect of state noise and measurement noise with a maximum magnitude e_0.

The magnitude of initial relative error $|\Delta g_0\%|$ and its numerator $|\Delta g_0\%|_n$ and denominator $|\Delta g_0\%|_d$ are then given by

$$|\Delta g_0\%| = \frac{|\Delta g_0|}{g_0 - 1} = \frac{|\hat{g}_0 - g_0|}{g_0 - 1} \triangleq \frac{|\Delta g_0\%|_n}{|\Delta g_0\%|_d}, \tag{39}$$

$$|\Delta g_0\%|_n = |e_1 F_{01}(F_{02} - F_{03}) + e_2 F_{02}(F_{03} - F_{01}) + e_3 F_{03}(F_{01} - F_{02})|, \tag{40}$$

$$|\Delta g_0\%|_d = (F_{01} + F_{03} - 2F_{02})\,[F_{02}(1 + e_2) - F_{03}(1 + e_3)]\,, \tag{41}$$

where as $|\Delta g_0\%|_n$ is a random number that cannot be intervened, the purpose of reducing $|\Delta g_0\%|$ can only be achieved by increasing $|\Delta g_0\%|_d$ through a reasonable selection of F_{0p} (i.e. i_p). As i_p has the same impact on the first factor of $|\Delta g_0\%|_d$ as on g_0 in Eq. (34), the preferred relationships of i_1, i_2 and i_3 here should also satisfy *Rule 2* and *Rule 3*. However, the second factor of $|\Delta g_0\%|_d$ is prone to reducing the gap between F_{02} and F_{03} based on *Rule 3*. If F_{02} has a similar value to F_{03}, the second factor will tend to zero and thus $|\Delta g_0\%|$ will tend to infinity. This will make the algorithm failed. Instead, F_{02} should exceed F_{03} to a significant extent to increase the safety margin of the second factor against noise. The lower limit is $F_{02} > F_{03} \cdot (1 + e_0)/(1 - e_0)$, which guarantees the second factor to be positive even if at the extreme case $e_2 = -e_0$ and $e_3 = -e_0$. (Note that this constraint is also applied in Eqs. (47) and (48)). Therefore, *Rule 3* is revised as below to balance the different requirements of the two factors of $|\Delta g_0\%|_d$.

$$Rule\ 3\ \text{(revised)}:\ i_2 <\approx i_3.$$

where the sign $<\approx$ denotes "slightly smaller". Similarly, the sign $>\approx$ denotes "slightly greater".

Next, let's examine the potential maximum magnitude of the initial relative error (denoted $|\Delta g_0\%|_{\max}$). Based on Eqs (40) and (41), the maximum numerator $|\Delta g_0\%|_n$ and minimum denominator $|\Delta g_0\%|_d$ are generated at the extreme case $e_1 = e_0$, $e_2 = -e_0$ and $e_3 = e_0$. Accordingly, $|\Delta g_0\%|_{\max}$ is given by

$$\begin{aligned} |\Delta g_0\%|_{\max} &= \frac{2e_0 F_{02}(F_{01} - F_{03})}{[(F_{02} - F_{03}) - e_0(F_{02} + F_{03})]\,(F_{01} + F_{03} - 2F_{02})} \\ &= \frac{2e_0}{\left[(1 - \frac{F_{03}}{F_{02}}) - e_0(1 + \frac{F_{03}}{F_{02}})\right] \cdot \left[1 - \frac{F_{02} - F_{03}}{F_{01} - F_{02}}\right] \Big/ \left[1 + \frac{F_{02} - F_{03}}{F_{01} - F_{02}}\right]}. \end{aligned} \tag{42}$$

To reduce $|\Delta g_0\%|_{\max}$, the values of the two factors of the denominator should be large; namely, the values of F_{03}/F_{02} and $(F_{02} - F_{03})/(F_{01} - F_{02})$ should be small. Evidently, *Rule 2* and *Rule 3* meet this requirement.

3.4. Selecting sampling points to reduce $|\Delta g_{Kt}|$

This subsection examines whether the gap between the actual and ideal curves can be shrinked as the increase of K_t under *Rules 1–3*. Define $a \triangleq il/K_t$, $b \triangleq (1 - e^{-a})/a$, g_{Kt} and $\hat{g}_{Kt}$ (the ideal and actual transient g-function values) are derived from Eqs. (7), (33) and (38) as

$$g_{Kt} = \left[\frac{F_{01}}{1 - b_1} - \frac{F_{02}}{1 - b_2}\right] \Big/ \left[\frac{F_{02}}{1 - b_2} - \frac{F_{03}}{1 - b_3}\right], \tag{43}$$

$$\hat{g}_{Kt} = \left[\frac{F_{01}(1 + e_1)}{1 - b_1} - \frac{F_{02}(1 + e_2)}{1 - b_2}\right] \Big/ \left[\frac{F_{02}(1 + e_2)}{1 - b_2} - \frac{F_{03}(1 + e_3)}{1 - b_3}\right], \tag{44}$$

https://doi.org/10.1017/S0263574715000739 Published online by Cambridge University Press

Δg_0 and Δg_{Kt} (the gaps between the curves at $K_t = 0$ and at an arbitrary K_t) are derived from Eqs. (34), (38), (43) and (44) as

$$\Delta g_0 = \hat{g}_0 - g_0 = \frac{(e_2 - e_3)F_{02}F_{03} + (e_3 - e_1)F_{03}F_{01} + (e_1 - e_2)F_{01}F_{02}}{(1 + e_2)F_{02}^2 + (1 + e_3)F_{03}^2 - (2 + e_2 + e_3)F_{02}F_{03}} \triangleq \frac{\Delta g_{0,n}}{\Delta g_{0,d}}, \tag{45}$$

$$\Delta g_{Kt} = \hat{g}_{Kt} - g_{Kt} = \frac{(e_2 - e_3)F_{02}F_{03} + \frac{1-b_2}{1-b_1}(e_3 - e_1)F_{03}F_{01} + \frac{1-b_3}{1-b_1}(e_1 - e_2)F_{01}F_{02}}{\frac{1-b_3}{1-b_2}(1 + e_2)F_{02}^2 + \frac{1-b_2}{1-b_3}(1 + e_3)F_{03}^2 - (2 + e_2 + e_3)F_{02}F_{03}}$$

$$\triangleq \frac{\Delta g_{Kt,n}}{\Delta g_{Kt,d}}. \tag{46}$$

As $W_2 \gg W_3$ and $i_2 <\approx i_3$ (see *Rule 1* and *Rule 3*), the relationships $F_{02} \gg F_{03}$ and $(1 + e_2)F_{02} \gg (1 + e_3)F_{03}$ can be satisfied in most cases (see Eq. (41) for an analysis). Thus, as proven in Eq. (47), the denominator of Δg_0 (denoted $\Delta g_{0,d}$) is positive.

$$\begin{aligned}\Delta g_{0,d} &= (1 + e_2)F_{02}^2 + (1 + e_3)F_{03}^2 - (2 + e_2 + e_3)F_{02}F_{03} \\ &= \underbrace{[(1 + e_2)F_{02} - (1 + e_3)F_{03}]}_{>0}\underbrace{[F_{02} - F_{03}]}_{>0} > 0.\end{aligned} \tag{47}$$

The denominator of Δg_{Kt} (denoted $\Delta g_{Kt,d}$) is expected to be positive too as proven in Eq. (48) based on the reasoning from *Rule 3* $i_2 <\approx i_3 \Rightarrow b_2 >\approx b_3 \Rightarrow \frac{1-b_2}{1-b_3} <\approx 1 <\approx \frac{1-b_3}{1-b_2}$,

$$\begin{aligned}\Delta g_{Kt,d} &= \frac{1 - b_3}{1 - b_2}(1 + e_2)F_{02}^2 + \frac{1 - b_2}{1 - b_3}(1 + e_3)F_{03}^2 - (2 + e_2 + e_3)F_{02}F_{03} \\ &\approx \underbrace{\left[\frac{1 - b_3}{1 - b_2}(1 + e_2)F_{02} - F_{03}\right]}_{>0}\underbrace{\left[F_{02} - \frac{1 - b_2}{1 - b_3}(1 + e_3)F_{03}\right]}_{>0} > 0.\end{aligned} \tag{48}$$

Next, let's examine the tendency of $(\Delta g_{Kt} - \Delta g_0)$ along with K_t. The denominator $(\Delta g_{Kt} - \Delta g_0)_d$ is positive since it is the product of $\Delta g_{0,d}$ and $\Delta g_{Kt,d}$ which are positive according to Eqs. (47) and (48). Therefore, the numerator $(\Delta g_{Kt} - \Delta g_0)_n$ determines the tendency of the gap. It is reasoned as below from the relationships $i_1 \gg i_2 \approx i_3$ and thus $b_1 \ll b_2 \approx b_3 < 1$.

$$\begin{aligned}(\Delta g_{Kt} - \Delta g_0)_n \approx\ & \underbrace{[(e_2 - e_3)F_{02}F_{03} + (e_3 - e_1)F_{03}F_{01} + (e_1 - e_2)F_{01}F_{02}]}_{\Delta g_{0,n}} \\ & \cdot \underbrace{\frac{b_1 - b_2}{1 - b_1}\left[(1 + e_2)F_{02}^2 + (1 + e_3)F_{03}^2\right]}_{<0} \\ & + \frac{b_1 - b_2}{1 - b_1}F_{02}F_{03}\left\{(1 + e_2)\left[(e_1 - e_3)F_{01}F_{03} - (e_2 - e_3)F_{02}^2\right]\right. \\ & \left. + (1 + e_3)\left[(e_1 - e_3)F_{01}F_{03} - (e_2 - e_3)F_{03}^2\right]\right\},\end{aligned} \tag{49}$$

where the first factor of the first item of the expression on the right side of the approximately equal sign is $\Delta g_{0,n}$, see Eq. (45). It has the same sign as Δg_0 because the denominator $\Delta g_{0,d}$ is positive as proven in Eq. (47). Further, the second factor of the first item is negative as $b_1 \ll b_2 < 1$. Therefore, the first item always has an opposite sign with Δg_0. This indicates the gap between the actual and ideal curves must shrink as the increase of K_t if the second item is ignored. Now, let's make a qualitative analysis to prove the impact of the second item on the gap tends to be smaller than that of the first item for the following reasons. First, both of the two terms are quartic polynomials of F_{0p} but the second item has less quartic terms than the first item (3 versus 6). Second, the first item is always able to

https://doi.org/10.1017/S0263574715000739 Published online by Cambridge University Press

shrink the gap as proven above, but the second item is functioned as random noise with approximately zero mean that may stochastically increase or decrease the gap.

3.5. Impact of track loads

Although all reasoning in Sections 3.2 to 3.4 is made under the hypothesis of the relationship of track loads $(W_2 - W_3)/(W_1 - W_2) = 1$, this ratio is not an essential condition of selecting sampling points. Instead, it is merely a coefficient in Eqs. (34), (38) and (43)–(47) that is not able to affect the reasoning philosophies, approaches and qualitative results of g_0, $|\Delta g_0\%|$ and $|\Delta g_{Kt}|$. Therefore, *Rule 1* is retained to simplify expression, whereas the equality relationship is changed to an approximate equality relationship to improve robustness of the rule against noise in sampling. The revised *Rule 1* is given by

$$Rule1(\text{revised}) : (W_2 - W_3)/(W_1 - W_2) \approx 1, \text{and} W_1 \gg W_2 \gg W_3.$$

3.6. Summary of sampling points selection

To sum up, three combinations of track load W_p and slip ratio i_p are required as input of the g-function algorithm for soil parameters identification. They are called "sampling points" because they are sampling centers to constitute the corresponding sample sets. Three rules are established to guide the selection of such sampling points on purpose of reducing the impact of noise on identification accuracy by enlarging the safety margin against noise, diminishing the magnitude of the initial error relative to the safety margin and narrowing the gap between the actual and ideal curves as the increase of K_t. These rules are given by

$$Rule1: (W_2 - W_3)/(W_1 - W_2) \approx 1, \text{ and } W_1 \gg W_2 \gg W_3;$$
$$Rule2: i_1 \gg i_2, \text{ at least } i_1 \geq i_2 \cdot W_1/W_2;$$
$$Rule3: i_2 <\approx i_3.$$

4. Sample Rearrangement

Although ideal relationships of the three sampling points (and thus the three sample sets) are qualitatively defined in the selection rules, yet for an individual sample, noise may be capable of causing the measurements to violate their ideal relationships. Therefore, we propose the operation of rearranging the samples in the order of increasing (or decreasing) F_p in each sample set as another technique to reduce the impact of noise on identification accuracy. The reason lies in that F_p is expected to be the main error source in the g-function algorithm as it contains not only its own measurement noise, but also state noise of the state variables transferred from Eqs. (4)–(6). After rearrangement, F_1, F_2 and F_3 will be all greater or smaller than their nominal values in most iterations of $g2$ and g-EKF calculation. Errors can thus be counteracted to a large extent by the subtraction calculations in Eqs. (7)–(9). This operation is not applicable to $g1$, whose input is the mean of the measurements that is irrelevant with sample sequence.

Sample distributions before and after the rearrangement operation are illustrated in Fig. 3. Each row represents a sample set, in which the six sub-plots refer to the original and rearranged F_p, W_p and i_p respectively. The fourth column (rearranged F_p) exhibits similar sample distributions in the three sub-plots as expected.

5. Flowchart for Soil Parameters Identification

5.1. A special case: pure clay

All reasoning in Section 3 is based on the hypothesis $F \propto W$ that is derived from Eq. (1). Although it is valid in most cases, there still exists an exception for pure clay with $\phi = 0$. On pure clay, F is independent with W and accordingly, selecting sampling points based on the established rules in

https://doi.org/10.1017/S0263574715000739 Published online by Cambridge University Press

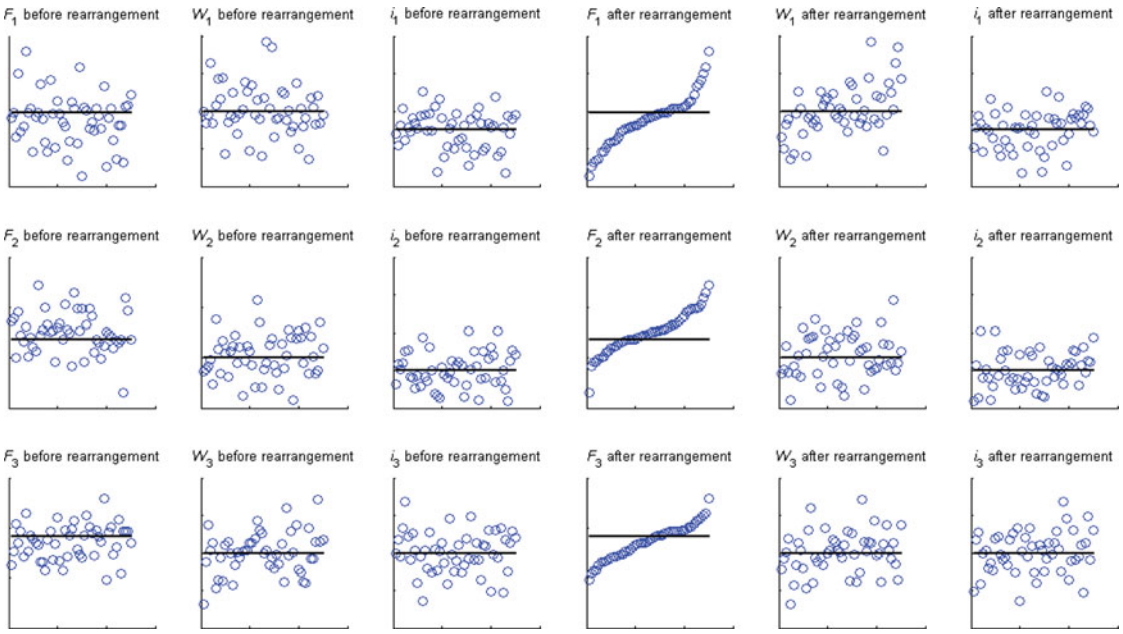


Fig 3. Sample distributions before and after rearrangement in the three sample sets.

Section 3 will receive an unexpected result $F_2 <\approx F_3$ (rather than $F_2 \gg F_3$ as usual) when $W_2 \gg W_3$ and $i_2 <\approx i_3$.

Therefore, the g-function algorithm and its variants as well as the selection rules of sampling points require an adjustment to fit for this special case. Since, only two soil parameters (c and K) need to be identified, the minimal number of sampling points correspondingly reduces to two. Each sampling point is denoted by a two-tuple array $[F_p, i_p]$, where i_p is the independent control variable and $p \in \{1, 2\}$. i_1 and i_2 are required to have a significant difference so as to keep the two sampling points away from each other (and thus to separate the two sample sets). Given $i_1 > i_2$ without a loss of generality, this requires i_2 slightly greater than 0 and i_1 big enough. However, two factors constrain the range of i_1 – first, the growth rate of F_1 decreases along with the increase of i_1 as $\partial^2 F/\partial i^2 < 0$ and second, an excessive increase of i_1 (especially when it exceeds a threshold $i_{\max}$) will amplify the danger of excessive subsidence and mobility loss of the track. Comprehensively, the selection rule of sampling points for pure clay is given by

$$\textit{Rule (for pure clay)} : W_1 \approx W_2,\ i_2 >\approx 0,\ i_1 \gg i_2,\ i_1 \le i_{\max}.$$

The g-function algorithm is modified as below based on Eqs. (7) and (9) with $\phi_{\text{est}} = 0$.

$$g(K_t) = \left[\frac{F_1}{[1 - \frac{K_t}{i_1 l}(1 - e^{-i_1 l/K_t})]}\right] \Bigg/ \left[\frac{F_2}{[1 - \frac{K_t}{i_2 l}(1 - e^{-i_2 l/K_t})]}\right], \tag{50}$$

$$c_{\text{est}} = \frac{1}{2A}\left(\frac{F_1}{[1 - \frac{K_{\text{est}}}{i_1 l}(1 - e^{-i_1 l/K_{\text{est}}})]} + \frac{F_2}{[1 - \frac{K_{\text{est}}}{i_2 l}(1 - e^{-i_2 l/K_{\text{est}}})]}\right). \tag{51}$$

$g1$, $g2$ and g-EKF all retain their procedures, but dimensions of related matrices and arrays in the EKF operator are reduced with the reduction of the number of soil parameters to be identified. For example, the extended ten-tuple measurement set z_{e1} in Eq. (25) is simplified to a seven-tuple set as below:

$$z_{\text{e1}} = [z_{\text{e}}^{\text{T}}, K]^{\text{T}} = [F_1, W_1, i_1, F_2, W_2, i_2, K]^{\text{T}}. \tag{52}$$

https://doi.org/10.1017/S0263574715000739 Published online by Cambridge University Press

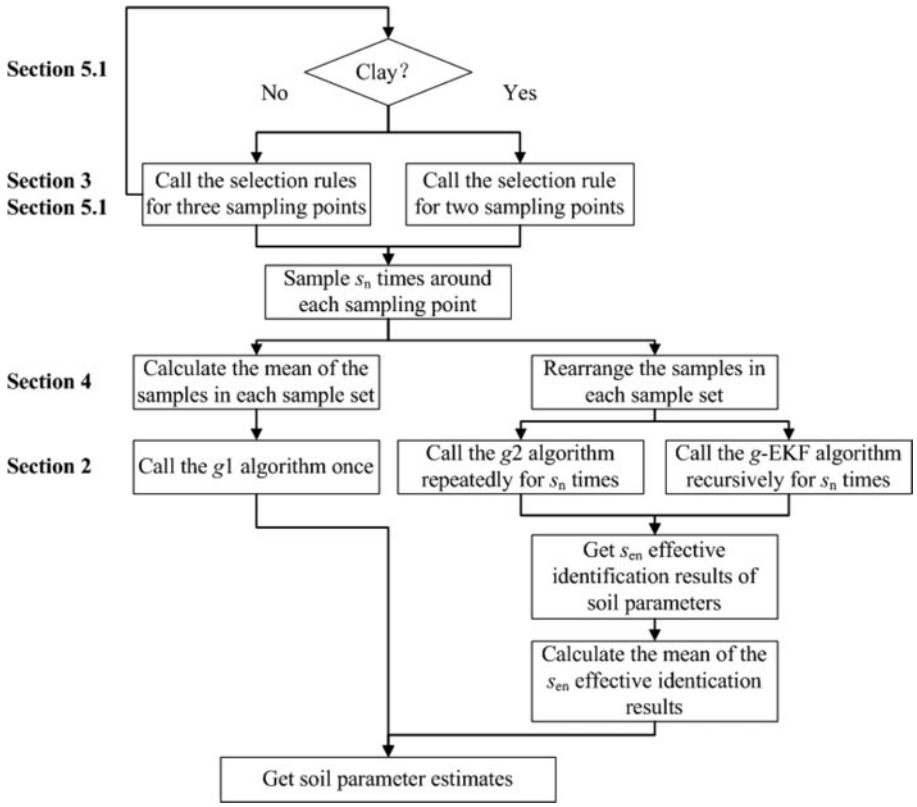


Fig 4. Flowchart for soil parameters identification.

It is worth pointing out the discussion of this special case is on purpose of maintaining the rigor of the algorithm, although clay is not a kind of targeted working terrain for most ACVs.

5.2. Flowchart for soil parameters identification

By synthesizing the contents in Sections 2, 3, 4 and 5.1, the complete identification process of the tractive-force-related soil parameters is presented in Fig. 4. It consists of seven steps: (1) adjusting track load and slip ratio in reasonable ranges and measuring the corresponding tractive force; (2) judging whether the soil is pure clay; (3) calling the corresponding rule(s) to select sampling points; (4) sampling repeatedly around each of the sampling points to constitute sample sets; (5) calculating the mean of the samples in each sample set for the $g1$ algorithm, or rearranging the samples in each sample set for the $g2$ or g-EKF algorithm; (6) calling $g1$, $g2$ or g-EKF to identify the soil parameters and (7) calculating the mean of the effective identification results as the final estimate of the soil parameters for $g2$ or g-EKF.

6. Experiments and Discussion

6.1. Experiment design

As referred to in Section 2.2, the g-function algorithm is applied to solve the multiple-solution problem in soil parameters identification by taking advantage of the ACV's degrees of control freedom in track load and longitudinal motion. Then, a series of de-noising techniques are proposed with respect to the g-function algorithm to solve the accuracy problem that is caused by state noise and measurement noise. These de-noising techniques consist of mean-effect strategies (i.e. averaging measurements for $g1$, averaging effective estimates for $g2$, as well as adjusting measurements recursively and averaging effective estimates for g-EKF), sampling points selection (for $g1$, $g2$ and g-EKF) and sample rearrangement (for $g2$ and g-EKF). Their effectiveness and robustness will be evaluated in

https://doi.org/10.1017/S0263574715000739 Published online by Cambridge University Press

Table I. Identification results of sandy loam at low levels of state noise and measurement noise.

		Final estimates			Relative errors of final estimates (%)			Standard deviations of relative estimation errors (%)		
Algorithm	s_{en}	$\overline{K_{est}}$(m)	$\overline{\tan\phi_{est}}$	$\overline{c_{est}}$(Pa)	$\overline{\delta(K_{est})}$	$\overline{\delta(tan\phi_{est})}$	$\overline{\delta(c_{est})}$	$\sigma(\delta(K_{est}))$	$\sigma(\delta(tan\phi_{est}))$	$\sigma(\delta(c_{est}))$
Nominal		0.0278	0.1944	5170						
$g1$		0.0278	0.19355	5189	0.000	−0.427	0.360			
$g2$	49	0.0278	0.19364	5190	−0.147	−0.380	0.386	6.381	2.954	2.905
g-EKF	48	0.0277	0.19362	5190	−0.225	−0.389	0.388	4.649	1.827	2.433

Table II. Identification results of sandy loam at a low level of state noise and a high level of measurement noise.

		Final estimates			Relative errors of final estimates (%)			Standard deviations of relative estimation errors (%)		
Algorithm	s_{en}	$\overline{K_{est}}$(m)	$\overline{\tan\phi_{est}}$	$\overline{c_{est}}$(Pa)	$\overline{\delta(K_{est})}$	$\overline{\delta(tan\phi_{est})}$	$\overline{\delta(c_{est})}$	$\sigma(\delta(K_{est}))$	$\sigma(\delta(tan\phi_{est}))$	$\sigma(\delta(c_{est}))$
Nominal		0.0278	0.1944	5170						
$g1$		0.0272	0.18784	5181	−2.158	−3.365	0.217			
$g2$	46	0.0266	0.18907	5000	−4.363	−2.734	−3.286	23.941	9.834	10.129
g-EKF	48	0.0270	0.18895	5196	−2.773	−2.794	0.495	11.807	3.926	7.995

this section by conducting three groups of experiment in different soil conditions and at different noise levels.

For soil conditions, typical sandy loam, dry sand and heavy clay are employed. Their nominal parameters are assigned values as:[3,19] $K_{nom} = 0.0278$ m, $\tan\phi_{nom} = 0.1944$, $c_{nom} = 5170$ Pa for sandy loam; $K_{nom} = 0.0512$ m, $\tan\phi_{nom} = 0.5317$, $c_{nom} = 1040$ Pa for dry sand; $K_{nom} = 0.006$ m, $\tan\phi_{nom} = 0.1051$, $c_{nom} = 20690$ Pa for heavy clay.

For noise levels, 1% stands for a low level of state noise or measurement noise, 10% stands for a high level of state noise, and 5% stands for a high level of measurement noise. They constitute four noise level combinations as: Level 1 with $n_x = 1\%$, $n_z = 1\%$; Level 2 with $n_x = 1\%$, $n_z = 5\%$; Level 3 with $n_x = 10\%$, $n_z = 1\%$; and Level 4 with $n_x = 10\%$, $n_z = 5\%$, where n_x and n_z denote state noise level and measurement noise level respectively.

For experimental condition, structural parameters of the prototype ACV presented in Fig. 1 are given by: the total weight of the vehicle $W_v = 2460$ N, the length of the tracks $l = 0.8$ m and the track-ground contact area $A = 0.152$ m^2. Software condition is MATLAB^{TM} R2008a in Windows^{TM} 7 using non-optimized code and hardware condition consists of an Intel® Core^{TM} i5-3230M CPU with 4.00 GHz of memory.

6.2. Evaluating the mean-effect strategies

Experiments in this subsection aim to evaluate $g1$, $g2$ and g-EKF for their mean-effect strategies, in terms of identification accuracy at different noise levels, performance stability in repeated tests and robustness to soil variation. The first two experiments are implemented on sandy loam and in the third experiment soil conditions extend to dry sand and heavy clay too.

6.2.1. Algorithm accuracy evaluation at different noise levels. Calculation results of $g1$, $g2$ and g-EKF at the four noise levels are presented in Tables I–IV respectively, in which the second column denotes the number of effective identification results, the next three columns denote the means of the effective identification results (i.e. the final estimates), the further next three columns denote the means of the relative estimation errors to the nominal values (i.e. relative errors of the final estimates) and the last three columns denote the standard deviations of the relative estimation errors. Further, to compare the performance of the three algorithms in a visualized manner, absolute values of the relative errors of the final estimates are presented in Fig. 5 that synthesizes the data in Tables I–IV. The following conclusions are drawn from the results:

https://doi.org/10.1017/S0263574715000739 Published online by Cambridge University Press

Table III. Identification results of sandy loam at a high level of state noise and a low level of measurement noise.

		Final estimates			Relative errors of final estimates (%)			Standard deviations of relative estimation errors (%)		
Algorithm	s_{en}	$\overline{K_{est}}$(m)	$\overline{\tan\phi_{est}}$	$\overline{c_{est}}$(Pa)	$\overline{\delta(K_{est})}$	$\overline{\delta(tan\phi_{est})}$	$\overline{\delta(c_{est})}$	$\sigma\ (\delta(K_{est}))$	$\sigma\ (\delta(tan\phi_{est}))$	$\sigma\ (\delta(c_{est}))$
Nominal		0.0278	0.1944	5170						
$g1$		0.0346	0.18220	5735	24.460	−6.267	10.922			
$g2$	34	0.0298	0.18435	5619	7.120	−5.158	8.676	24.154	15.047	11.938
g-EKF	33	0.0297	0.18337	5667	6.780	−5.664	9.619	23.625	14.523	10.476

Table IV. Identification results of sandy loam at high levels of state noise and measurement noise.

		Final estimates			Relative errors of final estimates (%)			Standard deviations of relative estimation errors (%)		
Algorithm	s_{en}	$\overline{K_{est}}$(m)	$\overline{\tan\phi_{est}}$	$\overline{c_{est}}$(Pa)	$\overline{\delta(K_{est})}$	$\overline{\delta(tan\phi_{est})}$	$\overline{\delta(c_{est})}$	$\sigma\ (\delta(K_{est}))$	$\sigma\ (\delta(tan\phi_{est}))$	$\sigma\ (\delta(c_{est}))$
Nominal		0.0278	0.1944	5170						
$g1$		0.0317	0.23491	6927	14.029	20.836	33.975			
$g2$	31	0.0238	0.20393	4799	−14.458	4.900	−7.178	33.048	22.240	13.393
g-EKF	36	0.0269	0.20059	5068	−3.397	3.186	−1.966	28.968	18.262	13.273

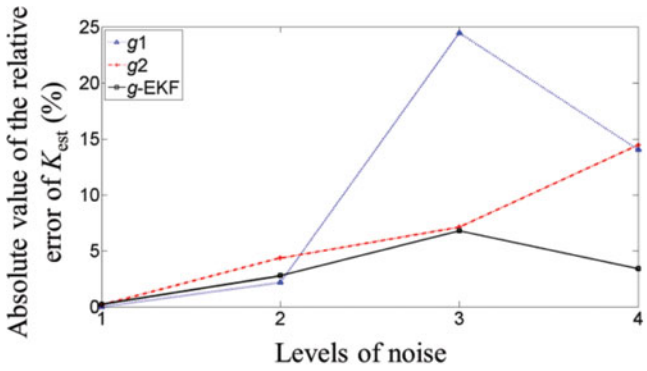
(1) g-EKF outperforms $g1$ and $g2$ in robustness to noise level variation. Although for all algorithms, identification accuracy is high at low levels of state noise and measurement noise (Level 1) but the accuracy reduces as the increase of noise, g-EKF has a broad applicability at all levels of noise with a comprehensive advantage in identification accuracy. Especially at high levels of state noise and measurement noise (Level 4) which are common in real environments,[7–9] g-EKF performs significant superiority over the alternatives.
(2) State noise and measurement noise have different impacts on $g1$ and $g2$. For $g1$, the difference between the results at noise Level 3 and the results at noise Level 1 is more significant than the difference between Level 2 and Level 1. This result indicates $g1$ is more sensitive to state noise than to measurement noise. Instead, $g2$ is equivalently sensitive to both kinds of noise as reflected from the experimental results. These phenomenon coincide with the theoretical analyses in Eqs. (10) and (11).

6.2.2. Algorithm stability evaluation in repeated tests. Ten trials of identification at high noise levels ($n_x = 10\%, n_z = 5\%$) are implemented by each algorithm to examine the stability of their performance. Statistical results are presented in Table V. Evidently, g-EKF outperforms $g1$ and $g2$ on the indices of data utilization ratio (number of effective identification results), accuracy (mean absolute values of the statistical parameters from the 10 trials, denoted $\delta(|^*|)$) and stability (standard deviations of the statistical parameters from the 10 trials, denoted $\sigma\ (^*)$). It is worth pointing out $g1$ gets two ineffective results in the 10 trials.

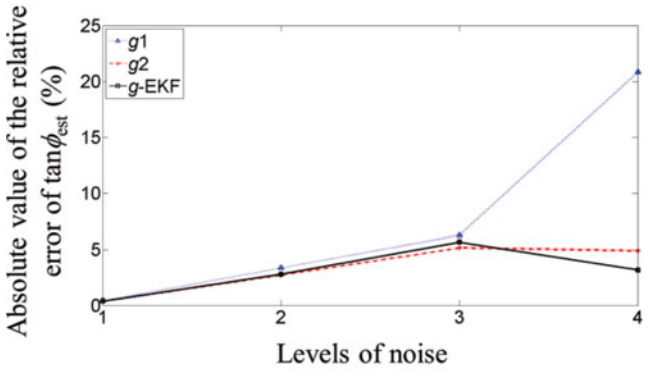
6.2.3. Algorithm robustness evaluation in different soil conditions. Apart from implemented at different noise levels, algorithm robustness evaluation is further implemented in different soil conditions in this experiment, including dry sand, sandy loam and heavy clay with significantly disperse parameter values and high-leveled noise. Taking relative estimation errors as the accuracy index, the results recorded in Table VI show g-EKF excels $g2$ that excels $g1$.

It is worth explaining the gross positive relative error of c_{est} on dry sand and that of $\tan\phi_{est}$ on heavy clay. As their nominal values (as safety margins against noise) are small, estimates with negative errors are vulnerable to be negative and thus be removed as ineffective identification results; instead, estimates with positive errors are tended to be preserved. Undoubtedly, the mean errors of effective identification results are positive. The reason of gross relative errors is attributed to the small nominal values too – even though absolute errors of the estimates are moderate.

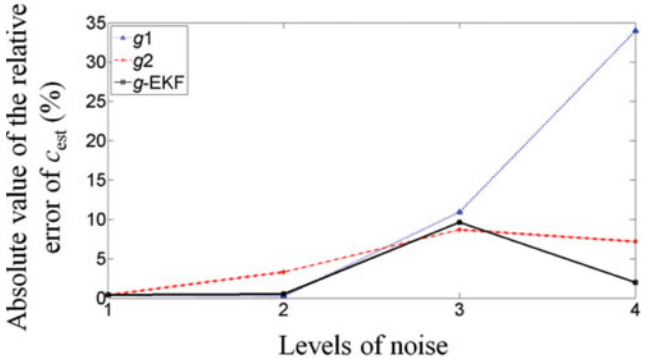
https://doi.org/10.1017/S0263574715000739 Published online by Cambridge University Press



(a) K



(b) $\tan\phi$



(c) c

Fig 5. Absolute values of the relative estimation errors of sandy loam parameters.

6.3. Evaluating the selection rules of sampling points

6.3.1. An example of sampling points selection. Given the six *W-i* pairs in Fig. 6 are sampled on sandy loam ($W_A = 970$ N, $i_A = 48\%$ at P_A; $W_B = 900$ N, $i_B = 30\%$ at P_B; $W_C = 730$ N, $i_C = 17\%$ at P_C; $W_D = 650$ N, $i_D = 23\%$ at P_D; $W_E = 490$ N, $i_E = 26\%$ at P_E; $W_F = 400$ N, $i_F = 32\%$ at P_F), they constitute the 20 sampling point combinations in Table VII. According to the selection rules established in Section 3, Combination 6 (P_A, P_C, P_E) is the best option.

Next, identification accuracy evaluation is implemented to these combinations to verify rationality of the selection rules.

https://doi.org/10.1017/S0263574715000739 Published online by Cambridge University Press

Table V. Statistical identification results of sandy loam from 10 trials at high noise levels.

Algorithm		Relative errors of final estimates (%) s_{en}	$\overline{\delta(K_{est})}$	$\overline{\delta(tan\phi_{est})}$	$\overline{\delta(c_{est})}$	Standard deviations of relative estimation errors (%) $\sigma(\delta(K_{est}))$	$\sigma(\delta(tan\phi_{est}))$	$\sigma(\delta(c_{est}))$
$g1$[b]	$\delta(\lvert*\rvert)$[a]		28.084	11.442	36.102			
	$\sigma(*)$[a]		37.295	10.601	25.472			
$g2$	$\delta(\lvert*\rvert)$	27.6	17.132	9.018	19.147	37.265	22.738	17.662
	$\sigma(*)$	6.91	22.413	11.475	16.730	12.004	9.531	7.965
g-EKF	$\delta(\lvert*\rvert)$	34.2	6.590	4.140	4.573	25.648	15.143	13.155
	$\sigma(*)$	4.05	8.364	4.619	5.290	5.002	4.158	3.325

[a]The operators denote calculating mean absolute value and standard deviation of the data from the 10 trials.
[b]Total failure happens twice in the 10 trials.

Table VI. Identification results of the three soil conditions at high noise levels.

Algorithm	Sandy loam (%) $\overline{\delta(K_{est})}$	$\overline{\delta(tan\phi_{est})}$	$\overline{\delta(c_{est})}$	Dry sand (%) $\overline{\delta(K_{est})}$	$\overline{\delta(tan\phi_{est})}$	$\overline{\delta(c_{est})}$	Heavy clay (%) $\overline{\delta(K_{est})}$	$\overline{\delta(tan\phi_{est})}$	$\overline{\delta(c_{est})}$
Nominal	0.0278 m	0.1944	5170 Pa	0.0512 m	0.5317	1040 Pa	0.006 m	0.1051	20690 Pa
$g1$	14.029	20.836	33.975	−19.057	18.552	110.77	32.909	81.264	−23.754
$g2$	−14.458	4.900	−7.178	12.003	−8.976	36.523	18.712	55.733	16.106
g-EKF	−3.397	3.186	−1.966	−5.190	4.924	9.358	8.317	20.801	−5.878

Table VII. Twenty combinations of sampling points.

Combination No	1	2	3	4	5	6	7	8	9	10	11	12	13	14	15	16	17	18	19	20
Sampling points	P_A	P_A	P_A	P_A	P_A	P_A	P_A	P_A	P_A	P_A	P_B	P_B	P_B	P_B	P_B	P_B	P_C	P_C	P_C	P_D
	P_B	P_B	P_B	P_B	P_C	P_C	P_C	P_D	P_D	P_E	P_C	P_C	P_C	P_D	P_D	P_E	P_D	P_D	P_E	P_E
	P_C	P_D	P_E	P_F	P_D	P_E	P_F	P_E	P_F	P_F	P_D	P_E	P_F	P_E	P_F	P_F	P_E	P_F	P_F	P_F
Condition number of $\partial F/\partial x$	105	405	458	125	71	48	41	137	69	122	98	59	51	150	76	133	186	183	3722	247

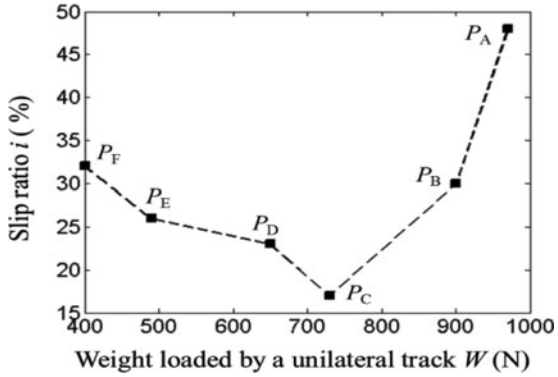


Fig 6. *W-i* pairs sampled on sandy loam.

6.3.2. Accuracy evaluation at different noise levels. As referred to in Section 3.1, the selection rules of sampling points are applicable to $g1$, $g2$ and g-EKF because they all employ the g-function algorithm as kernel. Without a loss of generality, only $g2$ is examined here for brevity and it is reasonable to assume the results of $g1$ and g-EKF are in the same tendency with $g2$.

https://doi.org/10.1017/S0263574715000739 Published online by Cambridge University Press

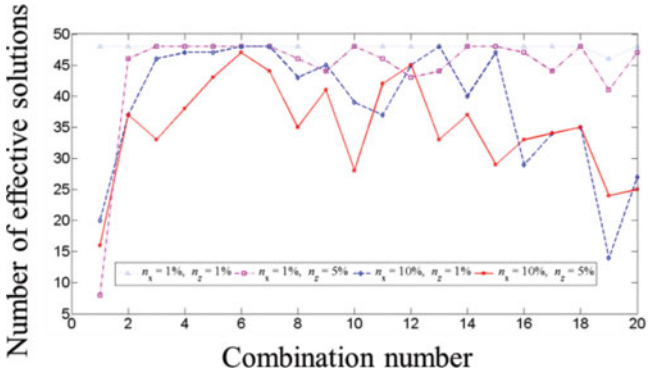


Fig 7. Data utilization ratio of the 20 combinations of sampling points.

This experiment is conducted on sandy loam at the four noise levels defined in Section 6.1. The results are shown in Figs. 7–9 in terms of data utilization ratio (number of effective identification results), accuracy (absolute mean values of the relative estimation errors) and stability (standard deviations of the relative estimation errors), respectively. The four curves in the figures correspond to the four noise levels, namely, dotted line for Level 1 with $n_x = 1\%$, $n_z = 1\%$, dash-dotted line for Level 2 with $n_x = 1\%$, $n_z = 5\%$, dashed line for Level 3 with $n_x = 10\%$, $n_z = 1\%$ and solid line for Level 4 with $n_x = 10\%$, $n_z = 5\%$. The following conclusions are drawn from the results:

(1) By synthesizing the seven indices in terms of data utilization ratio, identification accuracy and stability, Combination 6 (P_A, P_C, P_E) gets the best results. On the contrary, combinations with serious violation to the selection rules get poor results. They consist of Combinations 1, 17, 18, 19 and 20 for which W and i are in an approximately linear relationship, as well as Combination 11 for which the sampling points are located too close.
(2) Combinations 12 and 13 also get satisfied results although their ratios of track load differences are not approximately equal to one. This phenomenon indicates the ratio "1" defined in *Rule 1* is not an essential condition, coinciding with the theoretical analysis in Section 3.5.
(3) To further prove the accuracy of the above conclusions that are derived from qualitative reasoning, condition number of the Jacobian matrix $\partial F/\partial x$ is introduced as a quantitative index to evaluate the independence of Eqs. (4)–(6) regarding to each sampling point combination. As presented in Table VII, the computational result shows Combinations 6, 7, 12, 13 have the minimal condition numbers, which are thus denoted as best options. Evidently, the conclusion derived from quantitative calculation of condition number is the same as the conclusion derived from qualitative reasoning of selection rules. However, an inconformity happens at Combination 11 despite it is not among the worst options in the index "condition number" (the 8^{th} out of 20). The reason is, as the sampling points P_B, P_C, P_D are located too close, random noise is easy to weaken the theoretical independence of the equations that is derived from condition number calculation in an idealistic noise-free situation. This counter-example proves the quantitative calculation can only be used to validate and support the qualitative reasoning in Section 3 rather than replace it.
(4) Although both state noise and measurement noise are influential to identification accuracy (see Eq. (11) as the theoretical basis), the influence of state noise is relatively more significant. This conclusion is verifiable from the phenomenon that the dash-dotted line is located below the dashed line at most combinations in Figs. 7, 8(a) and 9.

6.4. Evaluating the operation of sample rearrangement

An experiment is conducted in this subsection to evaluate the operation of sample rearrangement by comparing the identification results of $g2$ and g-EKF with the operation versus their results without the operation. The experiment is implemented at the high noise levels ($n_x = 10\%$, $n_z = 5\%$) with ten trials in each condition. The statistical results are presented in Table VIII and analyzed as follows.

On the index "number of effective identification results", both $g2$ and g-EKF get a higher data utilization ratio with the sample rearrangement operation. However, they have different performances on the indices of accuracy (mean absolute values of relative estimation errors) and stability (standard

https://doi.org/10.1017/S0263574715000739 Published online by Cambridge University Press

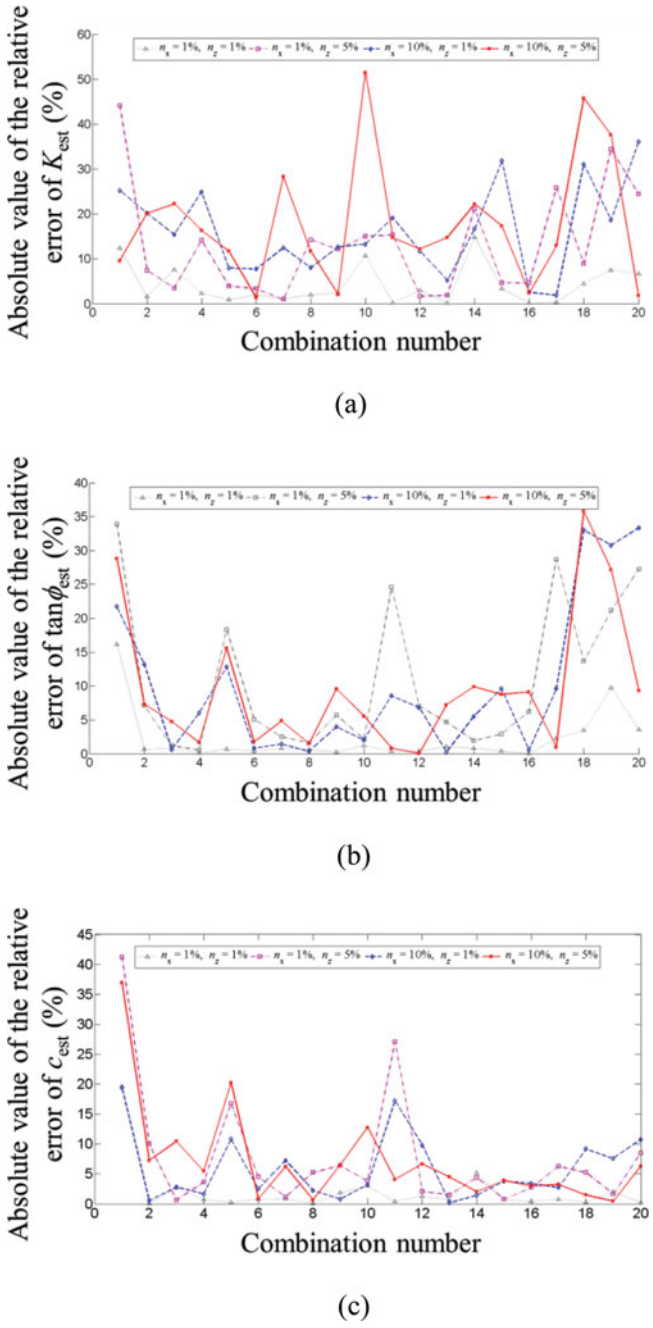


Fig 8. Identification accuracy of the 20 combinations of sampling points. (a) K, (b) tan ϕ and (c) c.

deviations of relative estimation errors) – sample rearrangement presents a more significant impact on g-EKF than on $g2$ on these indices. The reason is probably attributed to samples with gross noise, especially those with gross noise in different signs in F_p before rearrangement. In $g2$, their identification results are apt to be excluded as ineffective solutions, so that they only influence data utilization ratio rather than identification accuracy. Instead, in g-EKF, due to the error-averaging effect between iterations that is caused by the "measurement correction" operation, identification results of the samples with gross noise are able to be retained in a higher possibility (with significant but tolerable errors). Since these "imperfect" results are retained in the absence of sample rearrangement, the algorithm performances on identification accuracy and stability unavoidably get worsened.

https://doi.org/10.1017/S0263574715000739 Published online by Cambridge University Press

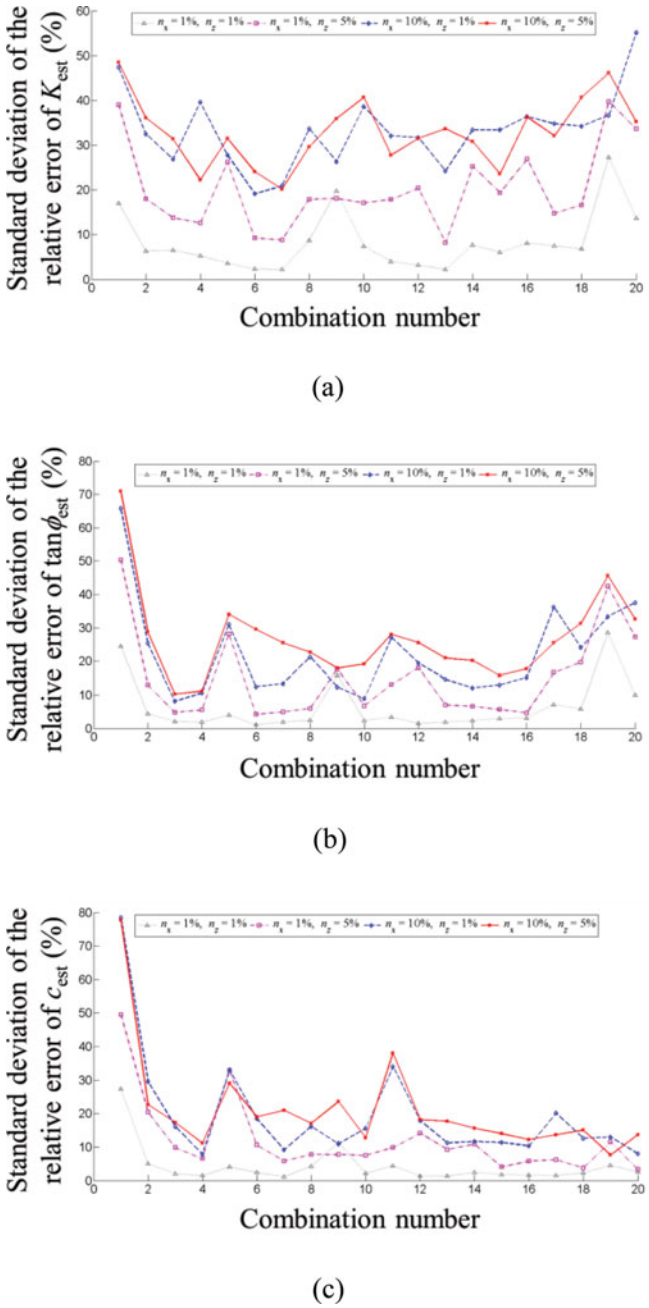


Fig 9. Identification stability of the 20 combinations of sampling points. (a) K, (b) tan ϕ and (c) c.

7. Conclusion

This paper studies on on-line inverse identification of the three tractive-force-related soil parameters for ACVs. A part of work is proposing the g-function algorithm to solve the multiple-solution problem by using ACVs' degrees of control freedom in track load and longitudinal motion. Another part of work is employing the de-noising techniques consisting of mean-effect strategies, sampling points selection and sample rearrangement to solve the accuracy problem. To be specific, for mean-effect strategies, their integration with the g-function algorithm constitutes the variants $g1$, $g2$ and g-EKF. For sampling points selection, qualitative rules are established to constrain parameter relationships of the three sampling points. For sample rearrangement, the samples are rearranged in the sequence of tractive force in each sample set on purpose of counteracting the noise by the subtraction calculations in the g-function algorithm. These techniques are evaluated by experiments conducted at different

https://doi.org/10.1017/S0263574715000739 Published online by Cambridge University Press

Table VIII. Statistical identification results of ten trials with and without sample rearrangement.

		With sample rearrangement				Without sample rearrangement			
		Relative errors of final estimates (%)				Relative errors of final estimates (%)			
Algorithm		s_{en}	$\overline{\delta(K_{est})}$	$\overline{\delta(tan\phi_{est})}$	$\overline{\delta(c_{est})}$	s_{en}	$\overline{\delta(K_{est})}$	$\overline{\delta(tan\phi_{est})}$	$\overline{\delta(c_{est})}$
g2	δ (|*|)[a]	27.6	17.132	9.018	19.147	22.8	18.593	10.057	15.136
	σ (*)[a]	6.91	22.413	11.475	16.730	3.59	15.937	14.424	16.850
g-EKF	δ(|*|)	34.2	6.590	4.140	4.573	27.4	11.469	7.034	3.695
	σ (*)	4.05	8.364	4.619	5.290	3.24	8.319	8.950	4.310

[a]The operators denote calculating mean absolute value and standard deviation of the data from the 10 trials.

noise levels and in different soil conditions. The experimental results coincide with theoretical analyses in terms of data utilization ratio, identification accuracy and performance stability.

As referred to in refs. [7–9], an important usage of soil parameters identification is as the precondition of vehicular operating performance optimization. Thus, the ongoing work tries to explore the impact of identification accuracy of soil parameters on energy consumption minimization based on this work and previous work on energy consumption modeling.[18]

Acknowledgements

This work was sponsored by National Natural Science Foundation of China project (61203351). It also benefited from helpful suggestions by the reviewers. Shuo Xu thanks Prof. D T Pham, Dr. Ze Ji, Dr. Dong Xie and Dr. Cong Ma for their help in discussion, advice and language revision.

References

1. M. G. Bekker, *Theory of Land Locomotion* (University of Michigan Press, Ann Arbor, 1956).
2. M. G. Bekker, *Introduction to Terrain-Vehicle Systems*, (University of Michigan Press, Ann Arbor, 1969).
3. J. Y. Wong, *Theory of Ground Vehicles*, 3rd ed. (John Wiley & Sons, Inc., New York, 2001).
4. S. Xu, C. Sun and D. Tu, "Step-by-step identification of soil parameters by air-cushion-typed off-road robots," *Chin. J. Mech. Eng.* **49**(9), pp. 1–11 (2013).
5. L. E. Ray, "Estimation of terrain forces and parameters for rigid-wheeled vehicles," *IEEE Trans. Robot.* **25**(3), pp. 717–726 (2009).
6. M. Wojciechowski, "Application of artificial neural network in soil parameter identification for deep excavation numerical model," *Comput. Assist. Mech. Eng. Sci.* **18**, pp. 303–311 (2011).
7. D. A. Dumond, L. Ray and E. Trautmann, "Evaluation of terrain parameter estimation using a stochastic terrain model," *Proc. SPIE – Int. Soc. Opt. Eng.* **7332**, pp. 73321F (2009).
8. L. Li and C. Sandu, "On the impact of cargo weight, vehicle parameters, and terrain characteristics on the prediction of traction for off-road vehicles," *J. Terramechanics*, **44**(3), pp. 221–238 (2007).
9. D. Golda, K. Iagnemma and S. Dubowsky, "Probabilistic Modeling and Analysis of High-Speed Rough-Terrain Mobile Robots," *Proceedings of the 2004 IEEE International Conference on Robotics and Automation (ICRA 2004)*, New Orleans, USA, (2004) pp. 914–919.
10. A. Tarantola, *Inverse Problem Theory and Methods for Model Parameter Estimation* (SIAM, Philadelphia, 2005).
11. S. Hutangkabodee, Y. H. Zweiri, L. D. Seneviratne and K. Althoefer, "Multi-solution problem for track-terrain interaction dynamics and lumped soil parameter identification," *Springer Tracts Adv. Robot.* **25**, pp. 517–528 (2006).
12. A. T. Le, D. C. Rye and H. F. Durrant-Whyte, "Estimation of Track-soil Interactions for Autonomous Tracked Vehicles," *Proceedings of the 1997 IEEE International Conference on Robotics and Automation (ICRA 1997)*, Albuquerque, USA, (1997) pp. 1388–1393.
13. K. Iagnemma, S. Kang, H. Shibly and S. Dubowsky, "Online terrain parameters estimation for wheeled mobile robots with application to planetary rovers," *IEEE Trans. Robot.* **20**(5), pp. 921–927 (2004).
14. S. Hutangkabodee, Y. H. Zweiri, L. D. Seneviratne and K. Althoefer, "Soil parameter identification for wheel-terrain interaction dynamics and traversability prediction," *Int. J. Autom. Comput. (IJAC)* **3**(3), pp. 244–251 (2006).

https://doi.org/10.1017/S0263574715000739 Published online by Cambridge University Press

15. L. Ding, H. Gao, Z. Deng, X. Libing, G. Junlong and Y. Lu, "An approach of identifying mechanical parameters for lunar soil based on integrated wheel-soil interaction terramechanics model of rovers," *Acta Aeronaut. Astronaut. Sin*. **32**(6), pp. 1112–1123 (2011).
16. L. Ding, H. Gao, Z. Deng, J. Tao and L. Xiong, "Wheel-soil interaction mechanics model for lunar rover: Decoupling and application," *J. Harbin Inst. Technol.* **43**(1), pp. 56–61 (2011).
17. L. Ding, K. Yoshida, K. Nagatani, H. Gao and Z. Deng, "Parameter Identification for Planetary Soil based on a Decoupled Analytical Wheel-Soil Interaction Terramechanics Model," *Proceedings of the 2009 IEEE/RSJ International Conference on Intelligent Robots and Systems (IROS 2009)*, St. Louis, USA, (2009) pp. 4122–4127.
18. S. Xu, J. Sun and J. Shen, "Energy consumption modelling for air-cushion vehicles," *Appl. Mech. Mater.* **483**, pp. 208–213 (2014).
19. S. Xu, Z. Luo, F. Yu, K. Zhou and Y. Zhang, "Slip ratio control simulation for semi-track air-cushion vehicle based on total power consumption minimization," *J. Syst. Simul.* **20**(16), pp. 4244–4247+4251 (2008).

https://doi.org/10.1017/S0263574715000739 Published online by Cambridge University Press